Journal of Failure Analysis and Prevention
https://doi.org/10.1007/s11668-026-02532-4

ORIGINAL RESEARCH ARTICLE

Measurement of Non-uniform Residual Stresses Using the Incremental Hole Drilling Method and Digital Image Correlation: A Feasibility Study on Deep Rolled Specimens

T. Grossi[1] · P. Neri[2] · C. Santus[2] · V. Colla[1]

Received: 30 March 2026 / Accepted: 29 May 2026

Abstract
This study explores the applicability of digital image correlation (DIC) techniques for measuring non-uniform residual stresses using the incremental hole drilling method. Specifically, it examines the residual stresses induced by a deep rolling treatment on 7075-T6 aluminum specimens, characterized by strong depth gradients. The aim is to assess the potential of replacing traditional strain gauge rosettes with DIC systems. After the deep rolling treatment, residual stresses were measured using the classic hole drilling method with a strain gauge rosette according to ASTM E837, providing a reference for the DIC measurements. The specimens and camera were mounted on a CNC machine, which allowed precise repositioning of both elements at each drilling step. Experimental results show that DIC measurements allow for the calculation of residual stresses with good accuracy. While their precision is lower than traditional strain gauge measurements, full-field DIC techniques partially compensate for this disadvantage by measuring the entire deformation field around the hole. This approach offers statistically advantageous data redundancy and captures displacements in areas immediately surrounding the hole, which are more sensitive to residual stresses. Considering the time and cost savings by avoiding the use of strain gauge rosettes, DIC techniques offer a valid alternative for determining residual stresses with the hole drilling method. The key factor for their application lies in the ease of repositioning both the camera and the drill at each depth increment.

Keywords Residual stress · Hole-drilling · Digital image correlation · Full-field · Regularization

Introduction

Background

The hole-drilling method (HDM) is among the most widely adopted experimental techniques for near-surface residual stress characterization, valued for its semi-destructive nature and broad applicability across engineering materials. Conceived by Mathar [1] in the early twentieth century and subsequently codified in the ASTM E837 standard [2], the method acquired its modern analytical depth through the integral method developed by Schajer [3–5], which reconstructs depth-varying stress distributions from numerically computed calibration functions. A thorough survey of the relevant literature can be found in [6].

The standard is built around the strain gauge (SG) rosette configuration introduced by Rendler and Vigness [7]. SG measurements combine high sensitivity with a mature instrumentation base, but their setup cost and operator dependency make them less practical when many tests are required. Full-field optical methods—notably Electronic Speckle Pattern Interferometry (ESPI) [8–10] and Digital Image Correlation (DIC) [11–14]—bypass this limitation by recording displacement maps over the whole specimen surface. ESPI delivers exceptional sensitivity [15] but is practically confined to laboratory environments due to strict vibration isolation requirements. DIC, available in both 2D and 3D configurations [16–18], offers a more industrially viable alternative [19] at the cost of lower sensitivity.

Initial DIC implementations of the HDM were restricted to uniform stress assumptions [11, 12]; more recent work extended the framework to depth-varying profiles through the integral method [13, 20, 21].

✉ T. Grossi
tommaso.grossi@santannapisa.it

1 TeCIP Institute, Scuola Superiore Sant'Anna, Via Giuseppe Moruzzi, 1, 56124 Pisa, Italy

2 Dipartimento di Ingegneria Civile e Industriale, Università di Pisa, Largo Lucio Lazzarino, 56122 Pisa, Italy

Published online: 02 September 2026

Context and Contributions

The ASTM E837 standard provides users with calibration functions for a variety of specimen thicknesses and rosette types [22], together with a Tikhonov regularization procedure governed by the Morozov discrepancy principle [23]. When full-field methods replace the SG rosette, one straightforward strategy consists in extracting *virtual strain gauge* readings from the displacement maps and feeding them into the standard inversion pipeline [24]. This approach, however, discards most of the spatial information available in the full-field data and does not compensate for the sensitivity deficit of DIC relative to physical gauges.

When the full displacement field is used directly, two main inversion strategies are available. The first, originally proposed by Schajer and Steinzig for ESPI [9] and later adapted to DIC [21, 25], involves a sequential two-step procedure: displacement fields are first estimated by standard DIC algorithms and then integrated to conform to the strain-gauge formalism, enabling continued adherence to the ASTM standard. Although this approach benefits from being easy to implement with off-the-shelf DIC software, it involves two consecutive inversions, each introducing bias in a way that is not analytically quantifiable and may compromise the final stress estimate [18]. As demonstrated in [26–28], performing a single unified inversion—controlled by a single, well-defined regularization parameter—is generally preferable.

The second strategy, introduced by Baldi [13], solves a *single inverse problem* that identifies the residual stresses directly from the acquired images, maximizing the correlation between simulated and experimental images simultaneously over all available pixels and drilling steps. This classifies the algorithm among global DIC methods. Our work draws from this second approach, demonstrating that it can match strain gauge accuracy while enabling rational regularization and depth super-resolution. In addition, we introduce a gradient-magnitude-based selection of informative pixels within the correlation annulus so as to restrict the inversion to the most textured regions of the speckle pattern, which reduces the computational burden of the global DIC problem without degrading the quality of the identified stress profiles.

An important ingredient not addressed in [13] is the principled choice of the Tikhonov regularization parameter. In the strain-gauge context, the Morozov discrepancy principle [29]—which requires knowledge of the measurement noise level—can be successfully applied. We show that this is not the case with DIC, and we instead propose the L-curve criterion [30] as a practical and robust alternative.

A further contribution of this work concerns the spatial resolution of residual stress profiles along the depth. In the SG-based integral method, the number of identifiable stress coefficients is bounded by the number of drilling steps (three strain measurements per step yield at most $3n$ data points for n increments). With full-field methods, the data are massively over-determined even when the number of stress unknowns exceeds the number of drilling steps, opening the possibility of identifying higher-resolution stress profiles from a reduced number of images—what we term *depth super-resolution*.

Theory

Hole-Drilling Forward Problem

When a blind hole is drilled into a linearly elastic body under the assumption of purely elastic induced deformations, Bueckner's superposition principle [31] allows the problem to be reformulated: the original stress state can be recovered by applying tractions on the hole wall equal and opposite to the relaxed stresses, which produce the same surface displacements as the actual drilling operation and can be evaluated with standard FE tools. The central assumption is that residual stresses vary only with depth z and are approximately uniform over the lateral footprint of the hole in the xy plane.

Under the integral method [4], the stress component $\sigma_{xx}(z)$ is approximated as piecewise constant over a set of n depth intervals $[h_{i-1}, h_i]$:

$$\sigma_{xx}(z) = \sum_{i=1}^{n} s_{xx,i}\ \chi_{[h_{i-1},h_i]}(z) \tag{1}$$

and analogously for σ_{yy} and σ_{xy}, with stress coefficients $s_{yy,i}$ and $s_{xy,i}$. Alternative bases—linear splines [32–34] or polynomials (Power Series Method [4])—can be employed equally.

By the linearity of the problem and its axial symmetry, the surface displacement field resulting from a single basis function admits a Fourier decomposition containing only the constant and 2θ harmonics. In cylindrical coordinates, the adimensional displacement field takes the form [25]:

$$\begin{aligned}
\frac{u_r(r,\theta,h)}{D_0} &= \frac{1}{E}\Bigg[\frac{s_{xx}+s_{yy}}{2}a_r(r,h) \\
&\qquad + \left(\frac{s_{xx}-s_{yy}}{2}\cos(2\theta) + s_{xy}\sin(2\theta)\right) b_r(r,h)\Bigg] \\
\frac{u_\theta(r,\theta,h)}{D_0} &= \frac{1}{E}\Bigg[\Bigg(\frac{s_{xx}-s_{yy}}{2}\sin(2\theta) \\
&\qquad -2s_{xy}\cos(2\theta)\Bigg) b_\theta(r,h)\Bigg]
\end{aligned} \tag{2}$$

where a_r, b_r, b_θ are radial calibration functions, computed via FE simulations using Fourier elements (e.g., SOLID272 in ANSYS) that reduce the three-dimensional problem to an efficient 2D axisymmetric model [35]. The function a_r captures the response to equibiaxial loading, while b_r and b_θ describe the response to pure shear. Storing these functions as one-dimensional profiles in r rather than as full pixel-resolution maps provides significant memory savings [13].

To account for typical DIC measurement artifacts—whose magnitude is often non-negligible in the context of residual stress identification—rigid-body motions (translation $t_{x,j}$, $t_{y,j}$ and rotation ω_j for the j-th image) are linearly superimposed onto the physical displacements in the Cartesian frame. Together, the stress and artifact coefficients are stacked into a vector $\boldsymbol{s}$, and the full system of displacement responses is assembled into the linear relation:

$$\boldsymbol{A}\boldsymbol{s} = \boldsymbol{u} \tag{3}$$

where $\boldsymbol{A}$ contains the influence functions from FE analyses, and $\boldsymbol{u}$ gathers all displacements at *all pixel positions* and *hole depths*.

Global Eulerian DIC Formulation

In its continuous form [36], DIC seeks a kinematic transformation $\phi(\boldsymbol{x}, \boldsymbol{u}(\boldsymbol{x})) = \boldsymbol{x} + \boldsymbol{u}(\boldsymbol{x})$ such that the gray level conservation equation holds:

$$r(\boldsymbol{x}, \boldsymbol{u}(\boldsymbol{x})) = f(\boldsymbol{x}) - g \circ \phi(\boldsymbol{x}, \boldsymbol{u}(\boldsymbol{x})) = 0, \quad \forall \boldsymbol{x} \in \Omega \tag{4}$$

where f and g are the reference and deformed image intensities, respectively. Since Eq 3 already provides the displacement field as a function of the finite-dimensional coefficient vector $\boldsymbol{s}$, Eq 4 can be directly rewritten in terms of $\boldsymbol{s}$ alone:

$$r_j(\boldsymbol{x}, \boldsymbol{s}) = f(\boldsymbol{x}) - g_j \circ \phi_j(\boldsymbol{x}, \boldsymbol{s}) = 0, \quad \forall \boldsymbol{x} \in \Omega, \forall j \in [1 \dots n_{\text{steps}}] \tag{5}$$

so that image correlation is carried out simultaneously across all drilling steps. This classification corresponds to a global DIC method. We adopt an *Eulerian* formulation:

$$r_j(\boldsymbol{x}, \boldsymbol{s}) = f \circ \phi_j^{-1}(\boldsymbol{x}, \boldsymbol{s}) - g_j(\boldsymbol{x}) = 0, \quad \phi^{-1}(\boldsymbol{x}, \boldsymbol{u}) = \boldsymbol{x} - \boldsymbol{u}(\boldsymbol{x}) \tag{6}$$

This choice requires building the interpolation of the reference image f only once—rather than constructing n_{steps} separate interpolations of the individual deformed images—and confers an additional signal quality benefit: the reference image is free of drilling debris, making its interpolation and gradient estimates less noisy than those of the deformed images. The optimization problem is then:

$$\boldsymbol{s}^\dagger = \arg\min_{\boldsymbol{s}} \Theta(\boldsymbol{s}) \triangleq \arg\min_{\boldsymbol{s}} \|\boldsymbol{r}(\boldsymbol{s})\|^2 \tag{7}$$

where $\boldsymbol{r}(\boldsymbol{s})$ stacks the per-pixel residuals from all images. The gradient of Θ is:

$$\left(\frac{\mathrm{d}\Theta}{\mathrm{d}\boldsymbol{s}}\right)^T = -2\,\boldsymbol{r}(\boldsymbol{s})^T \left.\frac{\mathrm{d}f}{\mathrm{d}\boldsymbol{x}}\right|_{\boldsymbol{x}=\phi^{-1}(\boldsymbol{x},\boldsymbol{s})} \boldsymbol{A} \tag{8}$$

which requires only the interpolation of f and its gradient at non-integer pixel locations—both precomputed once before the iterative loop. Problem 7 is solved iteratively via the Gauss-Newton method [36], by approximating the Hessian as:

$$\boldsymbol{H} \approx 2\left(\frac{\mathrm{d}\boldsymbol{r}}{\mathrm{d}\boldsymbol{s}}\right)^T \left(\frac{\mathrm{d}\boldsymbol{r}}{\mathrm{d}\boldsymbol{s}}\right) \tag{9}$$

Gradient-Based Selection of Informative Pixels

Within the annular correlation domain, not all pixels contribute equally to the inversion: pixels located on spatially uniform regions of the speckle pattern carry little displacement information and can degrade the signal-to-noise ratio of the identified stress coefficients. To concentrate computation on the most informative pixels and reduce the total cost of the optimization, a gradient-based selection strategy is employed.

The image intensity gradient magnitude is evaluated at each pixel of the reference image f using Sobel operators S_x and S_y applied in the x and y directions:

$$\nabla I(\boldsymbol{x}) = \sqrt{\left(I * S_x\right)^2 + \left(I * S_y\right)^2} \tag{10}$$

where $*$ denotes discrete convolution. Pixels at or near the boundaries of speckle features exhibit the largest gradient magnitudes; these are precisely the locations where sub-pixel interpolation of the image is most informative and where displacement-induced intensity shifts are most detectable. Only pixels whose gradient magnitude exceeds a prescribed percentile threshold—computed exclusively within the annular domain—are retained for the optimization. The resulting binary mask is illustrated in Fig. 1 for a threshold at the 75th percentile, applied to the reference image of the reported experimental data as an example. All results reported in this paper were obtained with a 95th-percentile threshold, which retains the sharpest 5% of speckle edges and yields a substantial reduction in computational load.

Tikhonov Regularization and the L-Curve

The hole-drilling inverse problem is inherently ill-posed [26, 27]: unregularized solutions amplify measurement noise and are typically highly oscillatory. Following the convention of ASTM E837 [2], second-order Tikhonov regularization is

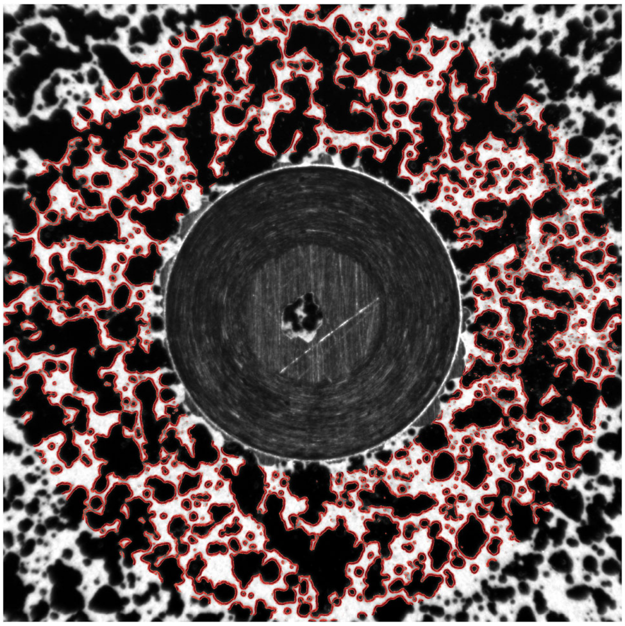

Fig. 1 Gradient-based pixel selection mask at a 75th-percentile threshold, applied to the reference image for the present analysis, reported as example. Red outlines mark speckle-pattern edges where gradient magnitudes peak and displacement sensitivity is highest

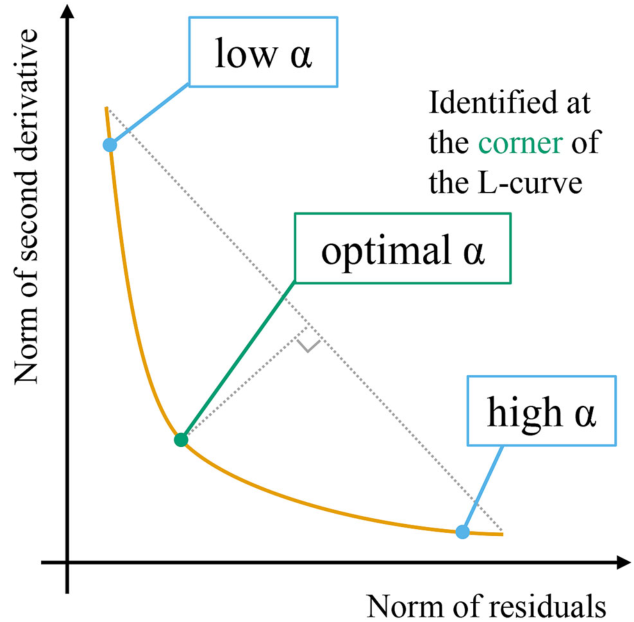

Fig. 2 Representative L-curve behavior. At low α, the residual is small but the solution is oscillatory (large second-derivative norm). At high α, the solution is smooth but the residual grows. The corner—identified as the point farthest from the chord connecting the endpoints—provides a robust operating point

applied by augmenting the objective function of Eq 7:

$$s_\alpha^\dagger = \arg\min_{s} \left[\Theta(s) + \alpha \, \|Cs\|^2 \right] \tag{11}$$

where C is the finite-difference matrix approximating the second derivative of the stress profile [26], and $\alpha > 0$ is the regularization parameter. The gradient of the regularized functional follows naturally from Eq 8:

$$\left(\frac{\mathrm{d}\Theta_\alpha}{\mathrm{d}s} \right)^T = -2\, r(s)^T \left. \frac{\mathrm{d}f}{\mathrm{d}x} \right|_{x=\phi(x,s)} A \; + \; 2\alpha \, s^T C^T C \tag{12}$$

Selecting α requires a principled criterion. In the SG context, the Morozov discrepancy principle [29] is effective: α is raised until the residual norm matches the expected value under the known measurement noise. We will show that this approach breaks down for DIC data, because the dominant contribution to the residual comes from drilling debris and localized paint damage—structured spatial artifacts unrelated to the stress signal—rather than from white noise, and their total magnitude changes very little across the entire practically relevant range of α values.

As an alternative, we adopt the *L-curve criterion* [30, 37, 38], which works as follows. Plotting $\sqrt{\Theta}$ against $\|Cs\|$ for a range of α values yields a characteristic L-shaped curve. Small α produces low residuals but noisy solutions; large α yields smooth solutions but high residuals. The corner of the L-curve—where a balance is achieved—provides a natural operating point. Rather than computing the curvature analytically (which requires high-order derivatives sensitive to numerical tolerances), we identify the corner as the point on the L-curve with *maximum distance from the straight line connecting its two endpoints* (see Fig. 2). A proof that this criterion is invariant under arbitrary linear rescaling of the axes—making it independent of the units in which residuals and penalties are expressed—is available in [39].

Algorithm Summary

The complete solution procedure unfolds as follows; a full step-by-step description is given in [39]. A reference image is captured at first contact of the drill tip with the specimen surface, and the hole center and radius are estimated by a Hough transform [40]. As proved in [34], the inverse problem has zero first-order sensitivity to small eccentricities when the correlation domain is symmetric about the hole axis, so the center identification need not be extremely precise. The number of stress basis functions is then selected and the FE calibration database [35] is queried to assemble A. A bicubic interpolation of the reference image is precomputed once [41]. The Gauss-Newton loop proceeds from a null initial guess, with image interpolations evaluated at non-integer pixel locations in each iteration. When the L-curve is required, the regularized problem is solved for a logarithmically spaced sequence of α values, each initialized from the converged solution at the previous α to reduce the total iteration count.

Super-Resolution Along Depth

In the SG-based integral method, the number of identifiable stress coefficients per component is at most equal to the number of drilling steps, since three strain values per step yield a total of $3n$ measurements for n increments. With full-field measurements, this constraint no longer applies: the pixel count far exceeds the number of stress unknowns, so the system remains strongly over-determined even when the number of stress coefficients exceeds the number of drilling steps.

The physical basis for this capability lies in how the calibration functions $a_r(r, h)$, $b_r(r, h)$, $b_\theta(r, h)$ vary with the depth of origin of the stress. At a given total hole depth h, stress contributions from shallow layers generate surface displacements concentrated close to the hole rim, whereas stress contributions from greater depths manifest over a broader radial extent [21]. From a functional analysis perspective, these depth-dependent radial profiles are linearly independent, allowing a single displacement image to be decomposed into contributions from distinct depth layers. The approach is limited solely by the ill-conditioning inherent in resolving contributions characterized by *near-collinearity*.

It is worth reframing this observation in terms of the physical mechanism that makes super-resolution possible. Every drilling step removes material from a finite depth interval, causing the entire overlying stress field to relax simultaneously. The resulting surface displacement field is therefore a superposition of contributions from all previously present stress layers. If those contributions are sufficiently linearly independent—as they are when the radial profiles corresponding to different depths are distinguishable—a single deformed image carries enough information to recover the individual layer contributions, provided that the measurement signal-to-noise ratio is adequate. In practice, achieving super-resolution beyond a certain ratio will be limited by the near-collinearity of calibration functions and by measurement noise, and the required accuracy currently exceeds the state of the art for high ratios. We investigate the feasibility of 1:2 and 1:5 super-resolution ratios in the experimental section.

Experimental Methods

Specimen and Deep Rolling Treatment

Residual stresses were introduced in a bar-shaped plate of 7075-T6 aluminum alloy by deep rolling. This alloy was chosen because of its combination of high yield stress, which permits large residual stress magnitudes, a linear elastic response within that range, and a relatively low Young's modulus, which translates surface deformations into larger absolute displacements, directly benefiting DIC sensitivity. The specimen geometry matched that used in earlier studies by the authors [42–46], purposely designed for a bending test bench that allows systematic validation of the hole-drilling measurements.

The deep rolling tool was a conical carbide roller pressed against the specimen surface. A built-in load cell and disk springs ensured a consistent normal force F_N, while the feed f controlled the spacing between successive passes. Parameters were set to $F_N = 150\,\mathrm{N}$ and $f = 0.1\,\mathrm{mm}$, consistent with prior studies [47, 48]. The resulting stress state is non-equibiaxial: compressive stresses in the feed direction exceed those in the rolling direction, with the affected zone extending approximately 0.4 mm below the surface.

Strain Gauge Reference Measurements

Reference residual stress profiles were obtained by the classical HDM using an HBM RY61K strain gauge rosette, mounted on the test bench equipped with a pneumatic actuator for applying and removing a calibrated bending load. By performing hole-drilling in both loaded and unloaded states, the bending-induced and residual strain contributions are decoupled; a detailed description of the bench and validation strategy is provided in [42]. The bending stress distribution serves as an independent check of the measurement quality: agreement between identified and applied bending stresses validates the experimental setup and excludes systematic errors.

Drilling was carried out with a 1.8 mm inverted cone bit (SINT Technology Restan, air turbine at over 300,000 rpm), reaching a maximum depth of 1.3 mm in 130 steps of 0.01 mm. Post-drilling, a hole diameter of 1.96 mm with negligible eccentricity was measured by the integrated optical microscope. Stress profiles were computed with linear spline basis functions, calibration coefficients from [32, 33, 49], and second-order Tikhonov regularization complemented by the Morozov discrepancy principle [26, 27].

DIC Setup on a CNC Machine

Accurate repositioning of both the camera and the drilling spindle after each increment is essential for HDM-DIC. Rather than using a dedicated rig [24], we exploit the high positioning repeatability of a CNC machining center (estimated at a few microns). Both the drill bit and the camera were mounted on the machine, with the camera rigidly attached to the stator portion of the spindle (non-rotating, but following all translational axes). This guarantees a fixed spatial relationship between the camera optical axis and the tool tip: after each drilling increment, the spindle retracts and

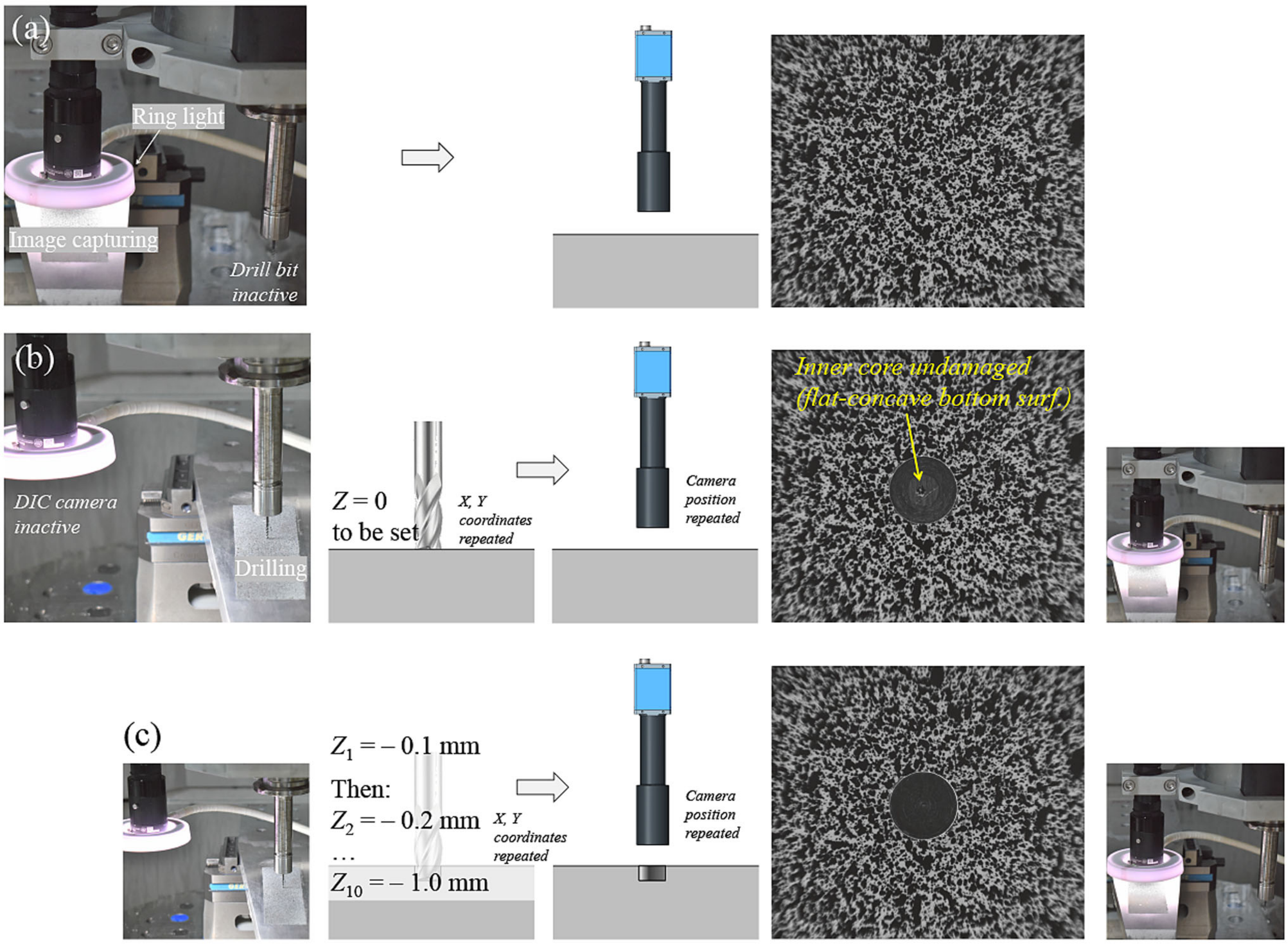

Fig. 3 Detailed experimental sequence on the CNC machining center: (**a**) camera repositioned for image capturing with active ring light; (**b**) drilling phase highlighting the critical zero-depth setting ($Z = 0$); (**c**) automated incremental procedure alternating between drilling and image acquisition at constant X, Y coordinates

the camera returns to the exact imaging position. A ring light mounted at the lens tip provided uniform illumination.

The camera and drill share a rigid frame so that the camera-to-tip distance vector remains constant throughout the test. As illustrated in the sequence in Fig. 3, the system alternates between the camera and the spindle while maintaining precise spatial alignment. Defining the Z-axis zero position relative to the plate surface is critical (Fig. 3b) [45]: the bit was rotated and lowered in 10 μm increments, with the reference image checked after each step for the first signs of surface contact; that depth was then set as zero. A reference image was captured at first contact; subsequent images were acquired after each 0.1 mm drilling increment, returning to the exact same X and Y coordinates for each capture (Fig. 3c).

The annular region used for correlation was defined between 1.1 and 2.1 times the hole radius in radial coordinate, capturing the highest-amplitude displacement response [50]. Within this annular domain, only pixels whose gradient magnitude exceeded the 95th-percentile threshold were retained for the optimization, following the strategy described in Gradient-Based Selection of Informative Pixels section. Drilling proceeded in 0.1 mm steps up to a nominal depth of 1.0 mm (measured depth 0.987 mm, hole diameter 2.015 mm). The optimization was run on an NVIDIA RTX 4090 GPU, which reduced the computation time from approximately ten minutes (CPU) to under one minute for the full analysis. A bicubic interpolation of the reference image was precomputed once using a cubic convolution algorithm [41], and iterative updates used a convergence tolerance of 10^{-6}. For the L-curve, Eq 11 was solved over $\alpha \in [10^{-3}, 10^{3}]$ on a logarithmically spaced grid, warm-starting each problem from the previous α solution. The key parameters of both HDM measurements are collected in Table 1 for reference.

Table 1 Summary of experimental parameters for the deep rolling treatment and both HDM measurements

Parameter	Value	Notes
Deep rolling treatment		
Material	Al 7075-T6	…
Normal force F_N	150 N	[47, 48]
Feed f	0.1 mm	[47, 48]
Strain gauge HDM		
Rosette	HBM RY61K	…
Drill bit diameter	1.8 mm	Inverted cone
Drilling system	SINT Restan	Air turbine, $>$ 300,000 rpm
Max. depth	1.3 mm	130 steps of 0.01 mm
Measured hole diameter	1.96 mm	Negligible eccentricity
Stress basis	Linear splines	[32, 33, 49]
DIC HDM		
Drill bit diameter	2.0 mm	Nominal
Drilling increment	0.1 mm	10 steps
Measured hole diameter	2.015 mm	Zeiss Calypso CMM
Annular ROI	1.1–2.1 r_{hole}	[50]
Zero-depth step size	10 µm	[45]
Gradient mask percentile	95%	See DIC Setup on a CNC Machine Section
Convergence tolerance	10^{-6}	Relative

Results and Discussion

The bending test bench was first used to validate the SG-based HDM measurement. The identified bending stress distribution agreed closely with the known applied load (Fig. 4a), with no observable surface bias from zero-depth identification errors [45], confirming the correctness of the experimental setup. From the same hole (unloaded state), the residual stress profiles were extracted (Fig. 4b). They exhibit the characteristic features of deep-rolled aluminum [47]: compressive stresses that are markedly anisotropic (larger in the feed direction), and a depth extent of approximately 0.4 mm.

Applying the proposed DIC algorithm without regularization confirms that the unregularized solution is highly oscillatory, consistent with the ill-posedness of the inverse problem [26]. The L-curve was computed over the range $\alpha \in [10^{-3}, 10^{3}]$; the corresponding L-curve is shown in Fig. 5. The L-curve corner criterion identifies $\alpha_{\text{L}} = 1.42$, while the value that minimizes the RMS deviation from the SG reference is $\alpha_{\text{opt}} = 1.07$. The corresponding solutions are shown in Fig. 6. The proximity of these two values is encouraging: it suggests that the L-curve provides a practically useful estimate without any knowledge of the ground-truth stress distribution.

Inspecting the L-curve (Fig. 5b) reveals that the residual norm changes by only a small amount over the entire tested range of α—spanning from clearly under-regularized to clearly over-regularized solutions. This behavior is in sharp contrast with the SG case, and can be attributed to the physical

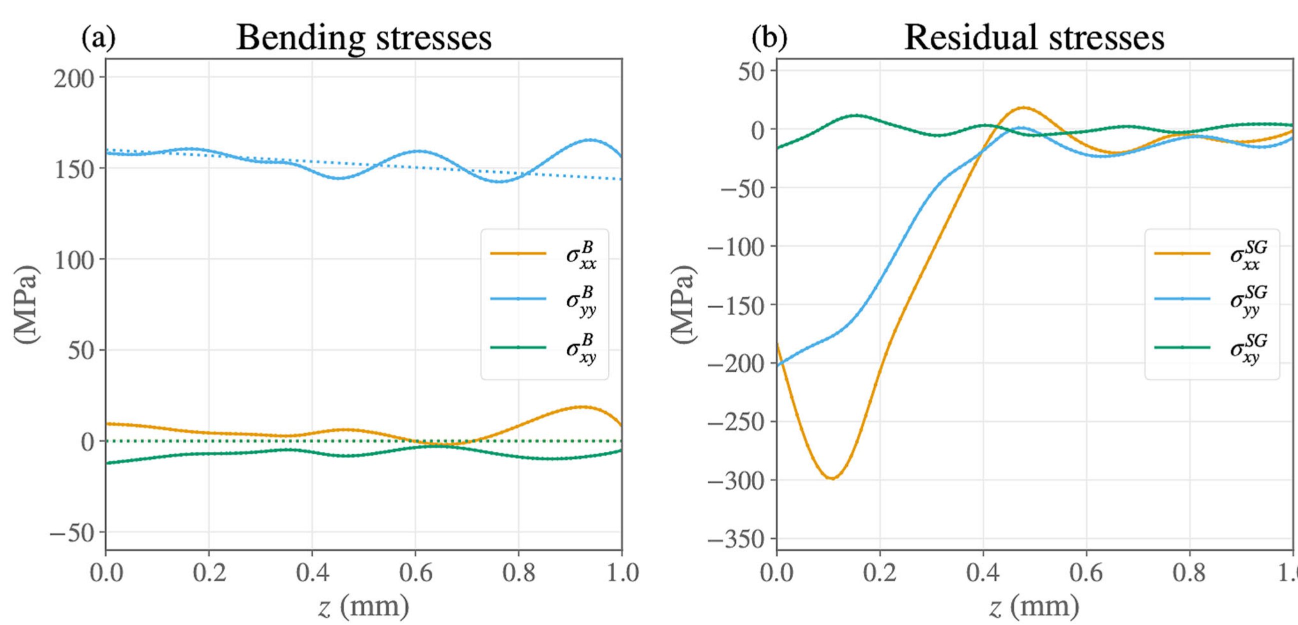

Fig. 4 (**a**) Bending stress profiles identified with the strain rosette on the test bench (solid lines) vs. applied values (dashed lines): close agreement confirms a correct experimental setup. (**b**) Residual stress distributions identified by the same rosette measurement

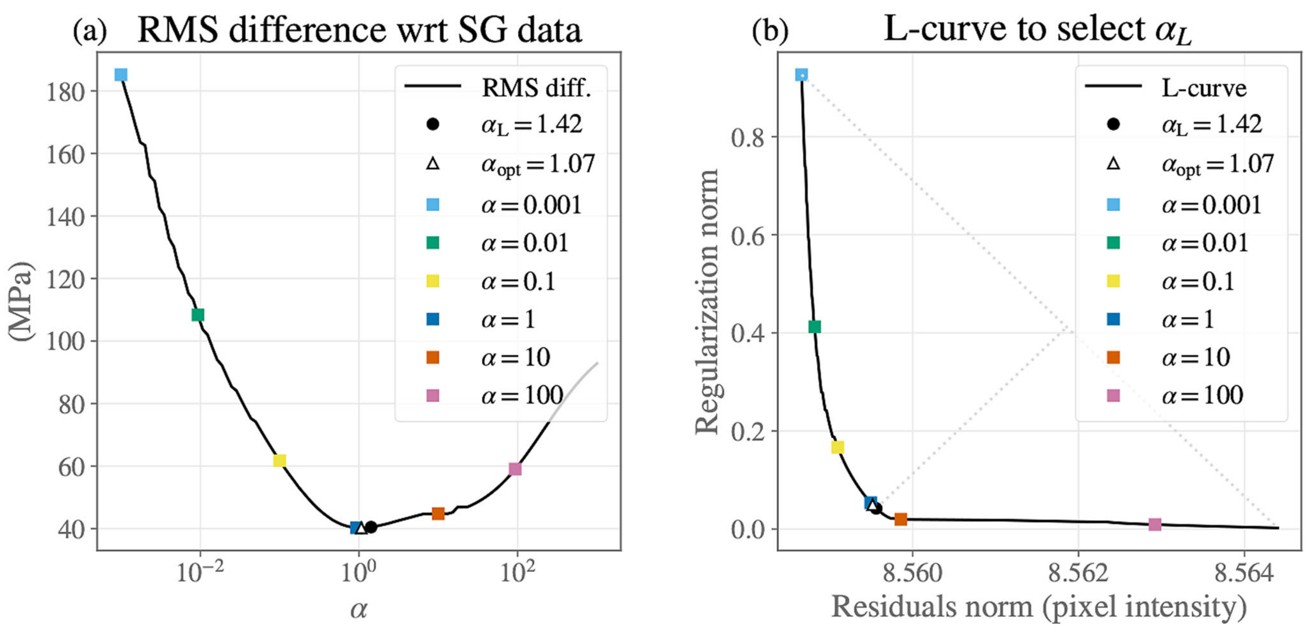

Fig. 5 (**a**) RMS discrepancy between DIC and SG solutions as a function of α; the L-curve corner ($\alpha_L = 1.42$) closely tracks the minimum ($\alpha_{opt} = 1.07$). (**b**) L-curve for the experimental case; the corner point is identified by maximum distance from the chord

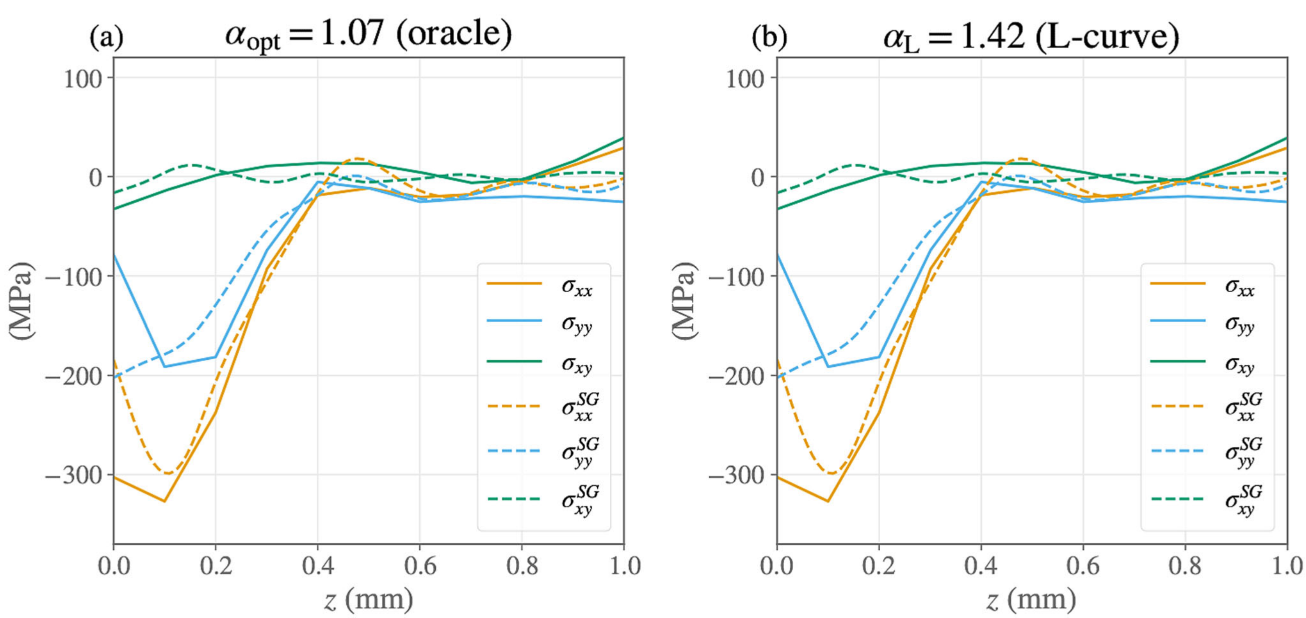

Fig. 6 Residual stress profiles: (**a**) DIC result at oracle regularization α_{opt} vs. SG reference; (**b**) DIC result at L-curve regularization α_L vs. SG reference. Both solutions are in close agreement with the strain gauge

nature of the dominant residuals: they arise from machining debris that entered the field of view despite compressed air cleaning, and from local damage to the painted surface (Fig. 7). These artifacts are spatially concentrated in a small fraction of pixels but carry large intensity differences (on an 8-bit scale), and their contribution to the residual norm is largely independent of the identified stress state.

The observed RMS residual of approximately 9 intensity levels is dominated by these outlier pixels, while the actual camera noise (measured by repeated captures of the same static scene) is approximately 4 levels. Since the degrees of freedom in $\boldsymbol{s}$ are orders of magnitude fewer than the total pixel count, even with $\alpha = 0$ the residual is already set by the debris contribution—not by the stress signal. Under these conditions, tuning α via the Morozov principle would require

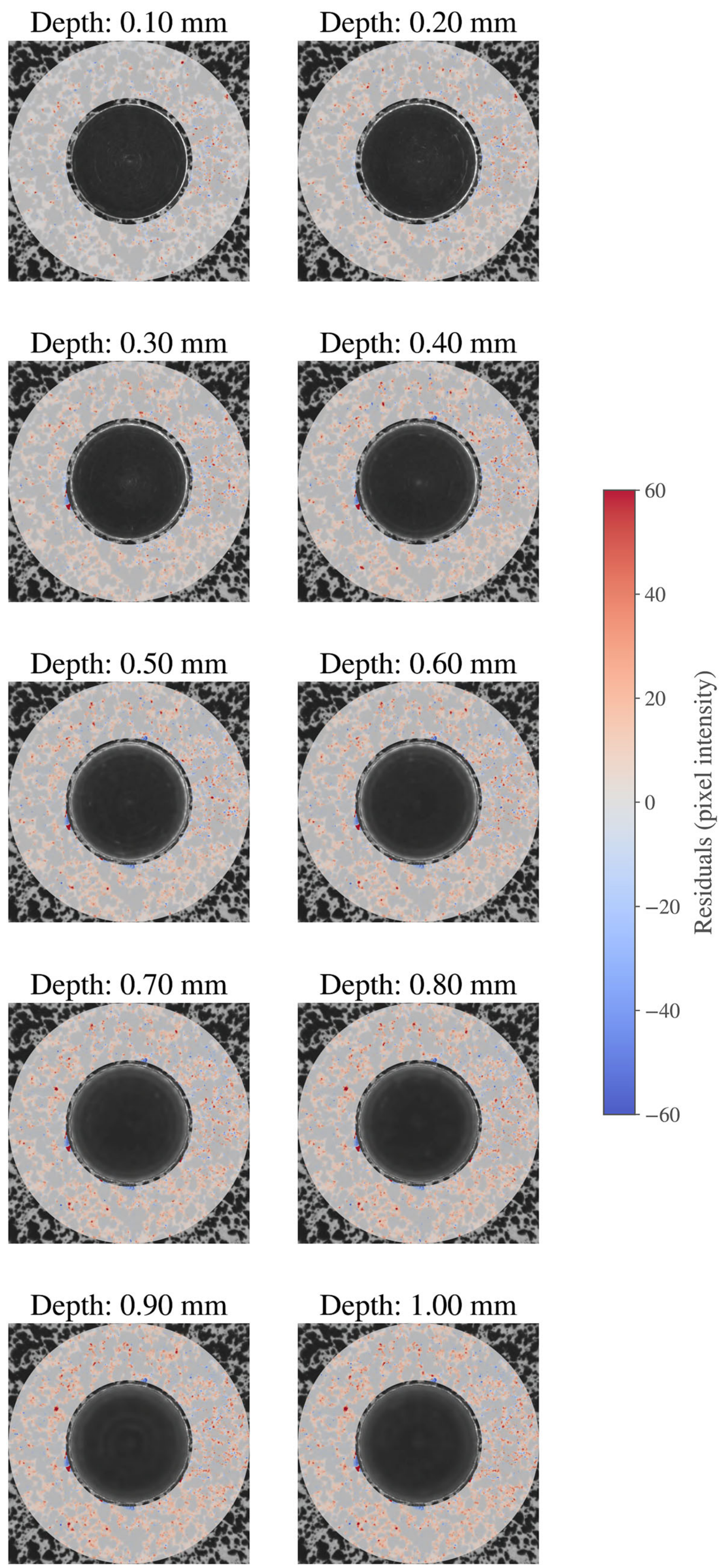

Fig. 7 Pixel-wise residuals between the experimental deformed images and the reconstructed ones, expressed as intensity differences (0–255). Elevated residuals are localized in small regions corresponding to debris and paint damage, on spatial scales much smaller than the displacement field

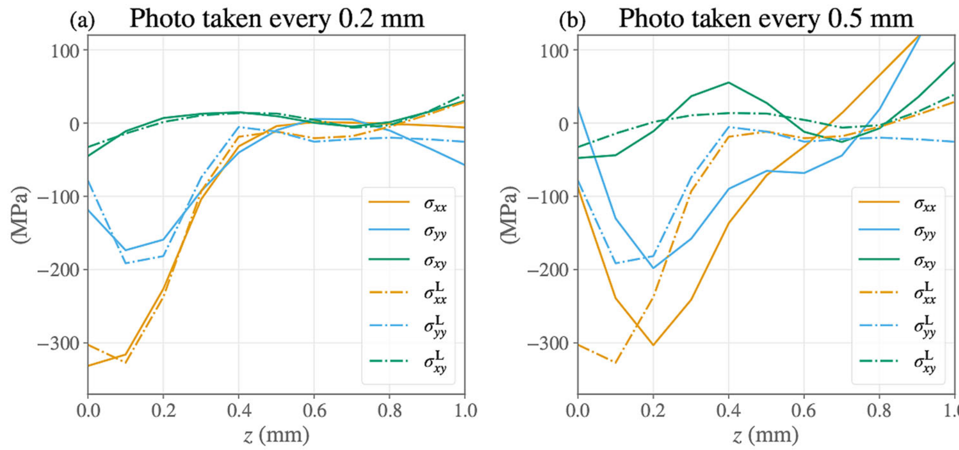

Fig. 8 Depth super-resolution results. The superscript L denotes the fully sampled reference case, obtained with regularization parameter α_L. (**a**) 1:2 ratio (5 images at 0.2 mm intervals): solution nearly indistinguishable from the fully sampled case. (**b**) 1:5 ratio (2 images only): the main trend is recovered, though accuracy decreases, particularly in the estimate of the stress decay depth

accurate knowledge of a measurement error that is neither white noise nor proportional to the stress-sensitive portion of the residual. The L-curve criterion, which requires no such prior information, is therefore a valid alternative.

To investigate the super-resolution capability, we repeated the identification using the full stress resolution (0.1 mm steps) but feeding only a subset of the acquired images: five images every 0.2 mm (1:2 ratio) and two images at 0.5 and 1.0 mm depth (1:5 ratio). The results are shown in Fig. 8.

The 1:2 case yields a solution whose degradation relative to the fully sampled result is negligible, confirming that halving the number of drilling steps is already feasible with current technology. The 1:5 case is more remarkable: with only two deformed images, the method still captures the general shape of the stress profile, including the sub-surface compressive peak in the feed direction, albeit with reduced accuracy in the stress decay region. These results quantify the practical trade-off between test duration and solution quality in a full-field HDM measurement, and paves the way for a concrete challenge for the residual stress community: achieving accurate stress depth profiles from a *single* reference and a *single* drilled image.

Conclusion

A global Eulerian DIC algorithm was proposed for the identification of non-uniform residual stress distributions from images acquired at incremental hole depths. The method solves a single inverse problem that directly relates raw images to residual stress coefficients, using an Eulerian image correlation framework and Tikhonov regularization. The main findings are as follows.

The L-curve criterion provides a practical and reliable tool for selecting the regularization parameter in HDM-DIC, overcoming the limitations of the Morozov discrepancy principle in the presence of spatially structured residuals from drilling debris. A CNC machining center can serve as an effective platform for automated HDM-DIC, ensuring sub-micron repositioning repeatability without dedicated rigs. The DIC-based identification produces residual stress profiles in close agreement with validated strain gauge measurements, both at the L-curve and near the oracle regularization levels. In addition, the gradient-magnitude-based pixel selection strategy introduced in this work concentrates the inversion on the most informative pixels in the annular correlation domain, significantly reducing the computational burden of the analysis while preserving the accuracy of the recovered stress profiles. Finally, depth super-resolution by a factor of two is practically achievable without noticeable loss of accuracy, while the 1:5 case still recovers the dominant features of the stress profile with only two images, opening perspectives for substantially shorter hole-drilling tests in industrial settings.

Conflict of interest The authors have no relevant financial or non-financial interests to disclose.

References

1. J. Mathar, Determination of initial stresses by measuring the deformations around drilled holes. Trans. Am. Soc. Mech. Eng. **56**(3), 249–254 (1934)

2. American Society for Testing and Materials, Test method for determining residual stresses by the hole-drilling strain-gage method. West Conshohocken, PA. (2020). https://doi.org/10.1520/E0837-20
3. G.S. Schajer, Application of finite element calculations to residual stress measurements. J. Eng. Mater. Technol. **103**(2), 157–163 (1981). https://doi.org/10.1115/1.3224988
4. G.S. Schajer, Measurement of non-uniform residual stresses using the hole-drilling method. Part I stress calculation procedures. J. Eng. Mater. Technol. **110**(4), 338–343 (1988). https://doi.org/10.1115/1.3226059
5. G.S. Schajer, Measurement of non-uniform residual stresses using the hole-drilling method. Part II practical application of the integral method. J. Eng. Mater. Technol. **110**(4), 344–349 (1988). https://doi.org/10.1115/1.3226060
6. G.S. Schajer, *Practical Residual Stress Measurement Methods*. (John Wiley & Sons, 2013)
7. N.J. Rendler, I. Vigness, Hole-drilling strain-gage method of measuring residual stresses: authors indicate that this method permits the magnitudes and principal directions of residual stresses at the hole location to be determined. Exp. Mech. **6**(12), 577–586 (1966). https://doi.org/10.1007/BF02326825
8. M. Steinzig, E. Ponslet, Residual stress measurement using the hole drilling method and laser speckle interferometry: Part 1. Exp. Tech. **27**(3), 43–46 (2003). https://doi.org/10.1111/j.1747-1567.2003.tb00114.x
9. G.S. Schajer, M. Steinzig, Full-field calculation of hole drilling residual stresses from electronic speckle pattern interferometry data. Exp. Mech. **45**(6), 526–532 (2005). https://doi.org/10.1007/BF02427906
10. G.S. Schajer, M. Steinzig, Dual-axis hole-drilling ESPI residual stress measurements. J. Eng. Mater. Technol. **132**(1), 011007 (2010). https://doi.org/10.1115/1.3184035
11. A. Baldi, Residual stress measurement using hole drilling and integrated digital image correlation techniques. Exp. Mech. **54**(3), 379–391 (2014). https://doi.org/10.1007/s11340-013-9814-6
12. J.S. Harrington, G.S. Schajer, Measurement of structural stresses by hole-drilling and DIC. Exp. Mech. **57**(4), 559–567 (2017). https://doi.org/10.1007/s11340-016-0247-x
13. A. Baldi, On the implementation of the integral method for residual stress measurement by integrated digital image correlation. Exp. Mech. **59**(7), 1007–1020 (2019). https://doi.org/10.1007/s11340-019-00503-5
14. Y. Peng, J. Zhao, L.-S. Chen, J. Dong, Residual stress measurement combining blind-hole drilling and digital image correlation approach. J. Constr. Steel Res. **176**, 106346 (2021). https://doi.org/10.1016/j.jcsr.2020.106346
15. A. Baldi, F. Bertolino, Sensitivity analysis of full field methods for residual stress measurement. Opt. Lasers Eng. **45**(5), 651–660 (2007). https://doi.org/10.1016/j.optlaseng.2006.08.010
16. D.V. Nelson, A. Makino, T. Schmidt, Residual stress determination using hole drilling and 3D image correlation. Exp. Mech. **46**(1), 31–38 (2006). https://doi.org/10.1007/s11340-006-5859-0
17. W.L. Gubbels, G.S. Schajer, Development of 3-D digital image correlation using a single color-camera and diffractive speckle projection. Exp. Mech. **56**(8), 1327–1337 (2016). https://doi.org/10.1007/s11340-016-0173-y
18. M. Hagara, F. Trebuňa, M. Pástor, R. Huňady, P. Lengvarský, Analysis of the aspects of residual stresses quantification performed by 3D DIC combined with standardized hole-drilling method. Measurement. **137**, 238–256 (2019). https://doi.org/10.1016/j.measurement.2019.01.028
19. H. Schreier, J.-J. Orteu, M.A. Sutton, *image Correlation for Shape, Motion and Deformation Measurements: Basic Concepts, Theory and Applications*. (Springer, Boston, MA, 2009) https://doi.org/10.1007/978-0-387-78747-3
20. J.D. Lord, D. Penn, P. Whitehead, The application of digital image correlation for measuring residual stress by incremental hole drilling. Appl. Mech. Mater. **13–14**, 65–73 (2008). https://doi.org/10.4028/www.scientific.net/AMM.13-14.65
21. G.S. Schajer, Optical hole-drilling residual stress calculations using strain gauge formalism. Exp. Mech. **61**(9), 1369–1380 (2021). https://doi.org/10.1007/s11340-021-00740-7
22. G.S. Schajer, Compact calibration data for hole-drilling residual stress measurements in finite-thickness specimens. Exp. Mech. **60**(5), 665–678 (2020). https://doi.org/10.1007/s11340-020-00587-4
23. G.S. Schajer, Hole-drilling residual stress profiling with automated smoothing. J. Eng. Mater. Technol. **129**(3), 440–445 (2007). https://doi.org/10.1115/1.2744416
24. E. Arabul, A.J.G. Lunt, A novel low-cost DIC-based residual stress measurement device. Appl. Sci. **12**(14), 7233 (2022). https://doi.org/10.3390/app12147233
25. G.S. Schajer, B. Winiarski, P.J. Withers, Hole-drilling residual stress measurement with artifact correction using full-field DIC. Exp. Mech. **53**(2), 255–265 (2013). https://doi.org/10.1007/s11340-012-9626-0
26. M. Beghini, T. Grossi, M.B. Prime, C. Santus, Ill-posedness and the bias-variance tradeoff in residual stress measurement inverse solutions. Exp. Mech. **63**(3), 495–516 (2023). https://doi.org/10.1007/s11340-022-00928-5
27. M. Beghini, T. Grossi, Towards a reliable uncertainty quantification in residual stress measurements with relaxation methods: finding average residual stresses is a well-posed problem. Exp. Mech. (2024). https://doi.org/10.1007/s11340-024-01066-w
28. M. Beghini, T. Grossi, Measuring residual stresses with crack compliance methods: an ill-posed inverse problem with a closed-form kernel. Appl. Mech. **5**(3), 475–489 (2024). https://doi.org/10.3390/applmech5030027
29. V.A. Morozov, *Methods for Solving Incorrectly Posed Problems*. (Springer, New York, NY, 1984) https://doi.org/10.1007/978-1-4612-5280-1
30. P.C. Hansen, *The L-Curve and its Use in the Numerical Treatment of Inverse Problems* (1999)
31. H.F. Bueckner, Novel principle for the computation of stress intensity factors. Z. Angew. Math. Mech. **50**(9), 5259 (1970)
32. M. Beghini, L. Bertini, L.F. Mori, Evaluating non-uniform residual stress by the hole-drilling method with concentric and eccentric holes. Part II: application of the influence functions to the inverse problem: eccentric influence functions—Part II. Strain. **46**(4), 337–346 (2010). https://doi.org/10.1111/j.1475-1305.2009.00684.x
33. M. Beghini, L. Bertini, L.F. Mori, Evaluating non-uniform residual stress by the hole-drilling method with concentric and eccentric holes. Part I definition and validation of the influence functions: eccentric influence functions—Part I. Strain. **46**(4), 324–336 (2010). https://doi.org/10.1111/j.1475-1305.2009.00683.x
34. M. Barsanti, M. Beghini, L. Bertini, B.D. Monelli, C. Santus, First-order correction to counter the effect of eccentricity on the hole-drilling integral method with strain-gage rosettes. J. Strain Anal. Eng. Des. **51**(6), 431–443 (2016). https://doi.org/10.1177/0309324716649529
35. M. Beghini, L. Bertini, M. Cococcioni, T. Grossi, C. Santus, A. Benincasa, Regularization of hole-drilling residual stress measurements with eccentric holes: an approach with influence functions. J. Mater. Eng. Perform. (2024). https://doi.org/10.1007/s11665-024-09447-x
36. J. Passieux, R. Bouclier, Classic and inverse compositional Gauss–Newton in global DIC. Int. J. Numer. Methods Eng. **119**(6), 453–468 (2019). https://doi.org/10.1002/nme.6057
37. P.C. Hansen, Analysis of discrete Ill-posed problems by means of the L-curve. SIAM Rev. **34**(4), 561–580 (1992). https://doi.org/10.1137/1034115

38. P.C. Hansen, *Discrete Inverse Problems: Insight and Algorithms*. (SIAM, 2010)
39. T. Grossi, P. Neri, C. Santus, Improved residual stress evaluation with hole-drilling and DIC through the L-curve tool and super-resolution along depth. Measurement. **258**, 119331 (2026). https://doi.org/10.1016/j.measurement.2025.119331
40. R.O. Duda, P.E. Hart, Use of the Hough transformation to detect lines and curves in pictures. Commun. ACM. **15**(1), 11–15 (1972). https://doi.org/10.1145/361237.361242
41. R. Keys, Cubic convolution interpolation for digital image processing. IEEE Trans. Acoust. Speech Signal Process. **29**(6), 1153–1160 (1981). https://doi.org/10.1109/TASSP.1981.1163711
42. M. Beghini, T. Grossi, C. Santus, E. Valentini, A calibration bench to validate systematic error compensation strategies in hole drilling measurements. In: *ICRS 11–11th International Conference on Residual Stresses* (2022) https://doi.org/10.36227/techrxiv.20347788.v1
43. M. Beghini, T. Grossi, C. Santus, A. Torboli, A. Benincasa, M. Bandini, *X-Ray Diffraction and Hole-Drilling residual Stress Measurements of Shot Peening Treatments Validated on a Calibration Bench*. (Italy, Milan, 2022)
44. M. Beghini, T. Grossi, C. Santus, L. Seralessandri, S. Gulisano, Residual stress measurements on a deep rolled aluminum specimen through X-ray diffraction and hole-Drilling, validated on a calibration bench. IOP Conf. Ser. Mater. Sci. Eng. **1275**(1), 012036 (2023). https://doi.org/10.1088/1757-899X/1275/1/012036
45. M. Beghini, T. Grossi, C. Santus, E. Valentini, Revealing systematic errors in hole drilling measurements through a calibration bench: the case of zero-depth data. J. Theor. Comput. Appl. Mech. (2023). https://doi.org/10.46298/jtcam.10080
46. M. Beghini, T. Grossi, C. Santus, Validation of a strain gauge rosette setup on a cantilever specimen: application to a calibration bench for residual stresses. Mater. Today Proc. (2023). https://doi.org/10.1016/j.matpr.2023.05.505
47. M. Beghini, L. Bertini, B.D. Monelli, C. Santus, M. Bandini, Experimental parameter sensitivity analysis of residual stresses induced by deep rolling on 7075–T6 aluminium alloy. Surf. Coat. Technol. **254**, 175–186 (2014). https://doi.org/10.1016/j.surfcoat.2014.06.008
48. L. Bertini, C. Santus, Fretting fatigue tests on shrink-fit specimens and investigations into the strength enhancement induced by deep rolling. Int. J. Fatigue. **81**, 179–190 (2015). https://doi.org/10.1016/j.ijfatigue.2015.08.007
49. M. Beghini, L. Bertini, Analytical expressions of the influence functions for accuracy and versatility improvement in the hole-drilling method. J. Strain Anal. Eng. Des. **35**(2), 125–135 (2000). https://doi.org/10.1243/0309324001514071
50. C. Santus, P. Neri, L. Romoli, M. Cococcioni, Residual stress determination with the hole-drilling method on FDM 3D-printed precurved specimen through digital image correlation. Appl. Sci. **14**(10), 3992 (2024). https://doi.org/10.3390/app14103992